Evolution of timing and spectral characteristics of 4U 1901+03 during its 2019 outburst using the *Swift* and *NuSTAR* observatories

Aru Beri [1,2]★ Tinku Girdhar,[1] Nirmal K. Iyer [3,4] and Chandreyee Maitra [5]

[1]*Indian Institute of Science Education and Research (IISER), Mohali, Punjab 140306, India*
[2]*Physics & Astronomy, University of Southampton, Southampton, Hampshire SO17 1BJ, UK*
[3]*KTH Royal Institute of Technology, Department of Physics, SE-106 91 Stockholm, Sweden*
[4]*The Oskar Klein Centre for Cosmoparticle Physics, AlbaNova University Centre, SE-106 91 Stockholm, Sweden*
[5]*Max-Planck-Institut für extraterrestrische Physik, Giessenbachstraße 1, D-85748 Garching, Germany*

ABSTRACT

We report the results from a detailed timing and spectral study of a transient X-ray pulsar, 4U 1901+03 during its 2019 outburst. We performed broadband spectroscopy in the 1–70 keV energy band using four observations made with *Swift* and *NuSTAR* at different intensity levels. Our timing results reveal the presence of highly variable pulse profiles dependent on both luminosity and energy. Our spectroscopy results showed the presence of a cyclotron resonance scattering feature (CRSF) at ∼ 30 keV. This feature at 30 keV is highly luminosity and pulse phase dependent. Phase-averaged spectra during the last two observations, made close to the declining phase of the outburst, showed the presence of this feature at around 30 keV. The existence of CRSF at 30 keV during these observations is well supported by an abrupt change in the shape of pulse profiles found close to this energy. We also found that 30 keV feature was significantly detected in the pulse phase-resolved spectra of observations made at relatively high luminosities. Moreover, all spectral fit parameters showed a strong pulse phase dependence. In line with the previous findings, an absorption feature at around 10 keV is significantly observed in the phase-averaged X-ray spectra of all observations and also showed a strong pulse phase dependence.

Key words: accretion – accretion discs – X-rays: individual: 4U 1901+03 – X-rays: binaries.

1 INTRODUCTION

A majority of accretion powered X-ray pulsars belong to the class of high mass X-ray binaries where the companion star is a Be-type star or an OB-type supergiant. Be-X-ray binaries (BeXRBs from now) are mostly transient systems that go into type I outburst close to the periastron passage and giant type II outbursts, which are rare (Reig 2011, and references therein). Transient X-ray pulsars are excellent candidates to understand changes in the accretion geometry and corresponding changes in timing and spectral signatures due to magnetically driven accretion (see e.g. Parmar, White & Stella 1989; Devasia et al. 2011; Maitra, Paul & Naik 2012).

4U 1901+03 (1901 from now) is a transient X-ray pulsar that was discovered with the *Uhuru* and *Vela 5B* observatories during its outburst in 1970–1971 (Forman, Jones & Tananbaum 1976; Priedhorsky & Terrell 1984). This source was classified as a BeXRB based only on its X-ray timing properties. The pulse period (P_{spin}) of 2.76 s (Galloway, Wang & Morgan 2005) and the orbital period (P_{orb}) of 22.6 d (Galloway et al. 2005; Jenke & Finger 2011; Tuo et al. 2020) placed it well in the region populated by BeXRBs of the $P_{orb} - P_{spin}$ diagram (Corbet 1986). This source was not detected in X-rays until February 2003, when the source underwent a second giant outburst that lasted for about 5 months (Galloway et al. 2005). During its 2003

outburst, the peak X-ray luminosity observed was ∼ 10^{38} ergs s^{-1} that changed by almost three orders of magnitude to 10^{35} ergs s^{-1}, assuming a distance of 10 kpc (Galloway et al. 2005). Later, this source was detected in outburst in 2011; however, this outburst was much shorter (1 month duration) and was fainter compared to its 2003 outburst with the peak X-ray luminosity of about **7 × 10^{36}ergs s^{-1}**, assuming source distance of 10 kpc (Sootome et al. 2011; Reig & Milonaki 2016). On February 8, 2019, 1901 was again detected in outburst with *MAXI*–GSC. This was recorded as the fourth outburst from this source in 40 yr (Hemphill et al. 2019; Mereminskiy et al. 2019; Nakajima et al. 2019) and lasted for about ∼160 d. During this outburst, several optical and X-ray observations were made and the peak X-ray luminosity measured during the 2019 outburst is about **1.4 × 10^{37}ergs s^{-1}**, assuming source distance of 3 kpc (Ji et al. 2020). Based on optical spectroscopy of the candidate Be star counterpart (B8/9 IV star), the source distance was proposed to be greater than 12 kpc (Strader et al. 2019; McCollum & Laine 2019). Tuo et al. (2020) using *Insight-Hard X-ray Modulation Telescope* (*Insight-HXMT*) data derived a similar value of the source distance. However, this is in contrast to that measured with *Gaia,* which suggests 1901 to be a nearby source at around $3.0^{+2.0}_{-1.1}$ kpc (Bailer-Jones et al. 2018).

The timing and spectral properties of 1901 were studied extensively during its previous bright outburst in 2003. (Galloway et al. 2005; Chen et al. 2008; Lei et al. 2009; James et al. 2011; Reig & Milonaki 2016). The pulse profiles showed complex morphology

Table 1. Observations made with *NuSTAR* and *Swift* during the 2019 outburst of 4U 1901+03.

	NuSTAR		
Obs ID	Exp time (ks)	Start time (MJD)	Pulse period (s)
90501305001 (Obs 1)	~44	58531.121	2.76288 ± 0.00003
90502307002 (Obs 2)	~38	58549.308	2.76154 ± 0.00003
90502307004 (Obs 3)	~54	58584.946	2.76211 ± 0.00004
90501324002 (Obs 4)	~102	58615.752	2.76075 ± 0.00003
	Swift		
Obs ID	Exp time (ks)	Start time (MJD)	Pulse period (s)
00088846001 (Obs 1)	~7	58531.768	2.7630 ± 0.0001
00088849001 (Obs 2)	~12	58549.426	2.7615 ± 0.0001
00037044015 (Obs 3)	~6.5	58581.052	2.7628 ± 0.0001
00088870001 (Obs 4)	~6.5	58615.774	2.7607 ± 0.0002

Note. The Gaussian 1σ uncertainties reported for the pulse periods were determined using the widths of the fitted Gaussian distributions to 'efsearch' results.

that were luminosity dependent (Lei et al. 2009; James et al. 2011). At high luminosity (above 10^{37}ergs s^{-1}), it showed a double-peak structure that changed to a single peak towards the end of the outburst. A quasi-periodic oscillation at 0.135 Hz was also detected in its light curves during 2003 outburst (James et al. 2011). A similar pulse profile evolution has also been found with the *NICER* and *Insight-HXMT* observations made during the 2019 outburst of 1901. These observations also revealed critical luminosity to be $\sim 10^{37}$ ergs s^{-1} (Ji et al. 2020; Tuo et al. 2020). Tuo et al. (2020) used value of the critical luminosity to estimate magnetic field of the neutron star in this system. Based on the accretion torque model, the authors suggested the value to be $\sim 4 \times 10^{12}$ Gauss.

The continuum X-ray spectra, observed with *Rossi X-ray Timing Explorer* (*RXTE*), were well modelled using an absorbed power law and exponential cutoff or a model consisting of thermal Comptonization component. A significant excess above 10 keV was also seen, indicating the presence of cyclotron resonance scattering feature (CRSF) in its X-ray spectra (Molkov, Lutovinov & Grebenev 2003; Galloway et al. 2005; James et al. 2011; Reig & Milonaki 2016). A pulse phase-resolved spectroscopy carried out by Lei et al. (2009) during the 2003 outburst indicated that the main pulse peak has the hardest spectrum. This is a common characteristic of an accreting X-ray pulsar (see e.g. Kreykenbohm et al. 1999; Maitra & Paul 2013). Moreover, 10 keV feature observed in the X-ray spectra of 1901 was also found to be strongly dependent on the X-ray flux and on the pulse phase (Reig & Milonaki 2016).

During the 2019 outburst of 1901, *Swift* and *NuSTAR* observations were made that allowed to study its broadband X-ray spectra (1–70 keV). The X-ray continuum was described with a combination of an absorbed blackbody and a power law with exponential cutoff (Coley et al. 2019; Mereminskiy et al. 2019). The iron emission line between 6 and 7 keV was also found in its X-ray spectrum (Coley et al. 2019; Jaisawal et al. 2019; Mereminskiy et al. 2019), in addition to the 10-keV feature (Coley et al. 2019; Mereminskiy et al. 2019). Moreover, one of the *NuSTAR* observations made close to the declining phase of the outburst revealed the presence of negative residuals in the X-ray spectra around 30 keV and this narrow absorption feature was interpreted as a CRSF (Coley et al. 2019).

Here in this paper, we report a detailed timing and spectral study of 1901 during its 2019 outburst. This paper is organized as follows. The observational data and procedure are described in the following section (Section 2). In Section 3, we describe the timing analysis while Section 4 is focused on the details on spectral analysis. In Section 5, we discuss the timing and spectral results obtained.
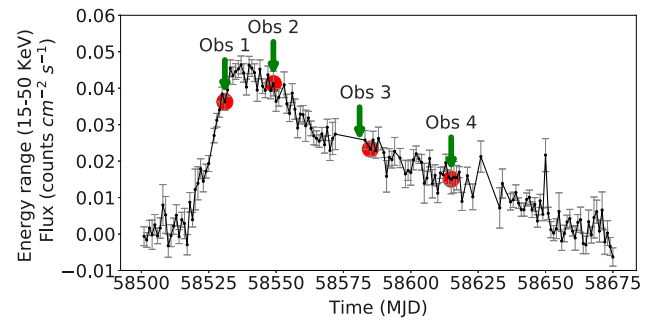

Figure 1. This plot shows the *Swift*-BAT light curve of 4U 1901+03 during its 2019 outburst. The red dots and green arrows indicate dates during which the *NuSTAR* and *Swift* observations were made, respectively.

2 OBSERVATIONS AND DATA ANALYSIS

During the 2019 outburst of 1901, four *NuSTAR* observations were performed, as detailed in Table 1. Fig. 1 shows the Swift–Burst Alert Telescope (BAT) light curve of 1901. We have marked times during which the *NuSTAR* observations were made. We have also marked *Swift* observations that were contemporaneous to these *NuSTAR* observations.

HEASOFT v6.19 and NUSTARDAS (V1.9.1) were used for standard processing and the extraction. The light curves, spectra, and the response files were extracted using NUPRODUCTS. A circular region of 100 arcsec radius for the source and a source-free circular region of 100 arcsec radius on the same chip for the background files were used.

We have used data obtained with XRT onboard Neil Gehrels *Swift* (see Table 1 for details). These XRT observations were performed in the windowed timing (WT) mode due to high source count rate. XRTPIPELINE was used to reprocess the data and using XSELECT source and background light curves and spectral files were generated. In order to avoid possible spectral residuals in the spectra, we have used grade 0 events and the source events were obtained from a circular region using 47$''$ radius. For the background events, the outer source-free regions were used, with a circular region of same radius as that used for the extraction of source events.

3 TIMING ANALYSIS AND RESULTS

3.1 Average pulse profiles

We extracted background and source light curves with a bin size of 100 ms in the energy band of 0.3–10 keV and 3–79 keV using data
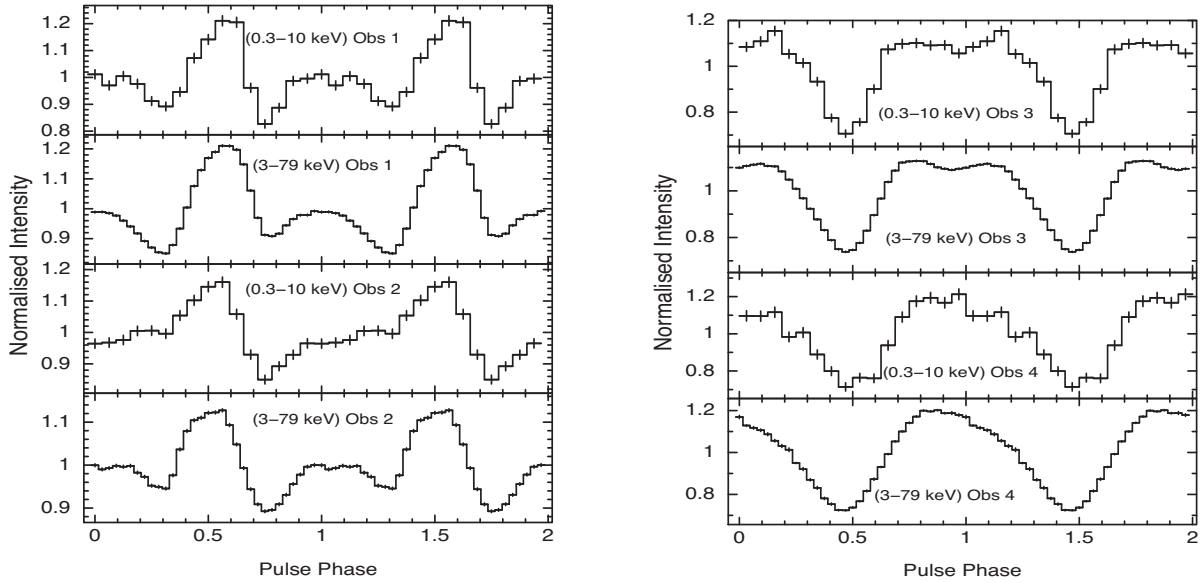
Figure 2. Average background subtracted pulse profiles obtained with (top to bottom) the XRT and *NuSTAR* data for Obs 1 and Obs 2 (left) whereas in the right plot, we show pulse profiles for Obs 3 and Obs 4. Error bars represent 1σ uncertainties. For plotting purposes, the profiles in different observations were aligned together (refer text for details).

of *Swift*-XRT and *NuSTAR*, respectively. Barycentric correction was applied to the background subtracted light curves using 'barycorr',[1] FTOOL task of HEASOFT. We searched for X-ray pulsations using the FTOOL task '*efsearch*' (see Table 1). As each observation spanned less than 5 per cent of the orbital period, the expected pulse smearing due to the change in pulse period is negligible. We performed a correction for smearing due to the orbital motion, using the ephemeris obtained from *Fermi*–GBM and found no change in the shape of pulse profiles. Therefore, we ignored it for rest of the analysis.

We folded *Swift*-XRT and *NuSTAR* light curves into 16 and 32 phase bins, respectively, with our measured periods (see Fig. 2). It can be observed that the pulse profiles showed a strong intensity dependence. During the rising phase of the outburst (Obs 1), both *Swift*-XRT and *NuSTAR* pulse profiles showed the presence of a primary peak and a secondary peak. Pulse profiles of both Obs 1 and Obs 2 have been shifted in pulse phase such that primary peak appears within 0.3–0.7 phase range. For Obs 2, the XRT pulse profiles did not show the presence of a secondary peak while this feature exist in the *NuSTAR* profiles, indicating energy dependence of pulse profiles (discussed in detail in the later section).

Towards the declining phase of the outburst, pulse profiles tend to be simpler (see right plot of Fig. 2). For Obs 3, both XRT and *NuSTAR* profiles exhibit broad shoulder-like structure while for Obs 4, the profiles tend to be sinusoidal. Here, again we have shifted all pulse profiles of Obs 3 and Obs 4 such that the dip occurs at phase 0.5.

3.2 Energy-resolved pulse profiles

To probe into the energy evolution of pulse profiles and pulsar emission geometry, we have folded energy-resolved light curves in different bands (see Figs 3–6).

For the rising phase observation (Obs 1), there exist a primary peak and a secondary peak in all the profiles below 12 keV; however,

it was found that above 12 keV, the secondary peak fades away and pulse profile tends to be a single peaked (see Fig. 3). For Obs 2, it was seen that XRT profiles are single peaked in all the energy bands while for the profiles created with *NuSTAR*, there is an evolution of the secondary peak with energy. At energies below 10 keV, profiles are more consistent with the structures observed with *Swift*–XRT while 10–12 keV band profile showed a presence of a secondary peak, which fades away with the increase in energy (see Fig. 4).

For Obs 3 (made during the declining phase of the outburst), we notice that pulse profiles in all the energy bands below 28 keV showed a broad shoulder-like structure. A drastic change was observed in the pulse profiles of 28–37 keV and 37–50 keV band. Pulse profile in the 28–37 keV band changed from single to twin-peaked. The first peak appeared at around 0.3 pulse phase while the second peak was seen around 0.7 phase. In the last energy band (37–50 keV), pulse profile again changed to single peaked profile with a disappearance of the second peak around 0.7 phase (see Fig. 5). Similar energy dependence was also seen in the pulse profiles of Obs 4 where all the profiles below 28 keV showed a sinusoidal behaviour. We observe that in the 28–37 keV band, pulse profile tend to show a sharper peak compared to rest of the energy bands and with some phase shift. Moreover, there is an emergence of a secondary peak between 0.7 and 0.8 pulse phase. It was interesting to notice that in comparison to the 28–37 keV band, the pulse profiles of 37–50 keV band showed a sharp peak between 0.6 and 1.0 pulse phase with a disappearance of twin-peaked behaviour (see Fig. 6).

Pulse fraction (PF) defined as the ratio between the difference of maximum (I_{max}) and minimum (I_{min}) intensity to their sum was estimated: $[(I_{max} - I_{min})/(I_{max} + I_{min})]$. We investigated the change in PF with energy for which we estimated PF in several energy ranges (see Fig. 7). The horizontal bars on data points in Fig. 7 represent the energy ranges in which PF has been estimated while the vertical bars represent errors on the PF in a given energy range. We found that for all observations, PF shows an increasing trend with energies up to 25 keV. For Obs 1, PF increased from
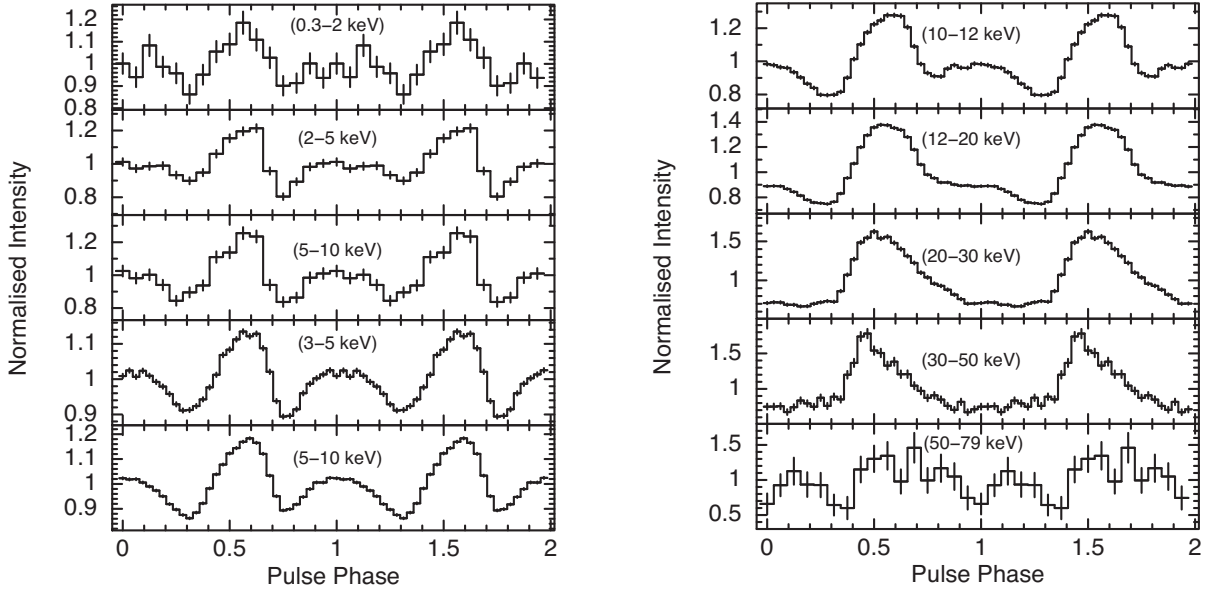
Figure 3. Energy-resolved pulse profiles of 4U 1901+03 obtained with the XRT (0.3–10 keV) and *NuSTAR* (3–79 keV) data during Obs 1.
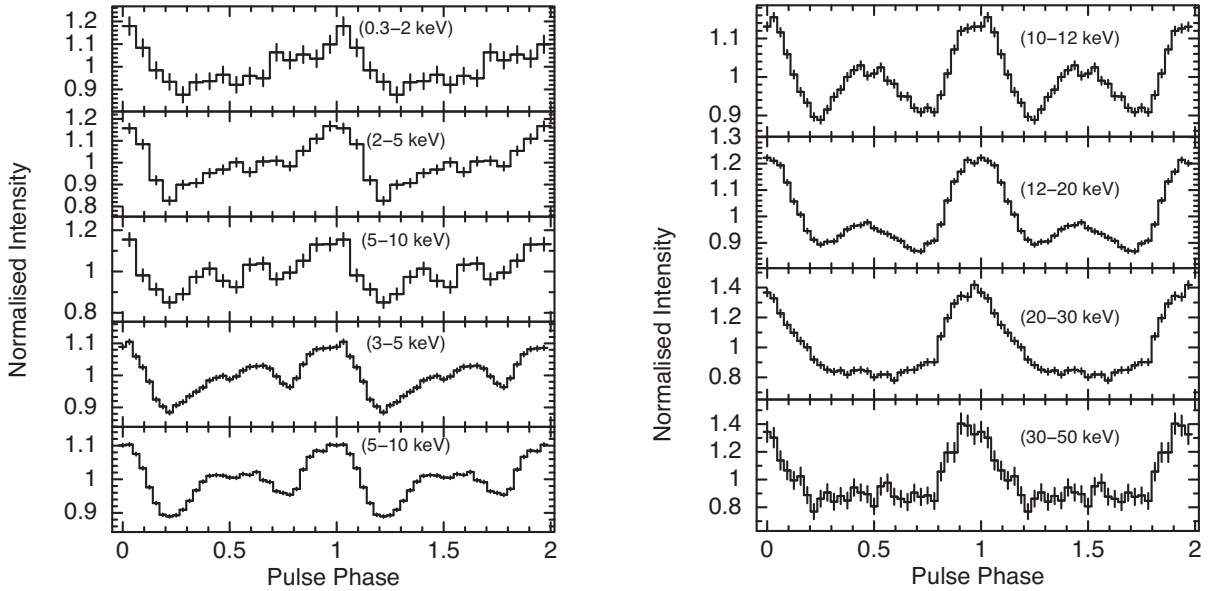

Figure 4. Energy-resolved pulse profiles of 4U 1901+03 obtained with the XRT (0.3–10 keV) and *NuSTAR* (3–79 keV) data during Obs 2.

11.9 ± 0.1 to 45.0 ± 3.0 per cent and for Obs 2, it increased from 11.1 ± 0.1 to 29.0 ± 2.0 per cent. PF showed values between 17.2 ± 0.2 and 55.0 ± 9.0 per cent during Obs 3 while for Obs 4, there was an increase from 20.0 ± 1.0 to 34.0 ± 2.0 per cent in the PF.

3.3 Hardness ratio

To track spectral evolution with the pulse phase, we have used a model independent way of creating hardness ratio (HR) plots. Fig. 8 shows phase-resolved HR. We computed two HR indices, HR1 and HR2. HR1 was calculated by taking ratio of count rates in 12–20 keV and 5–8 keV energy bands while HR2 was computed for count rate ratio between 30–50 keV and 12–20 keV energy band. HR was computed across 32 phase bins except for Obs 4 where

HR2 was computed using only 16 phase bins (due to the limited statistics).

We notice that HR plots for Obs 1 and Obs 2 are similar for both indices showing a single peaked profile, where the peak corresponds to the hard spectra. Comparing HR plots to the pulse profiles, it appears that peak of the HR plot corresponds to peak of the pulse profiles. For the case of Obs 3 and Obs 4, it is interesting to note that the peak of HR1 corresponds to the dip of HR2. The most intriguing aspect observed in Obs 3 is that HR2 profiles showed a twin-peaked behaviour, indicating significant changes in the HR or spectral behaviour of two HR indices, HR1 and HR2. Fig. 9 shows Hardness-Intensity diagrams obtained by plotting phase-resolved HR against normalized sum intensity in different energy bands. We observed a direct correlation between intensity and hardness in all except HR2 of Obs 4, suggesting an increase in hardness with the increase in intensity.
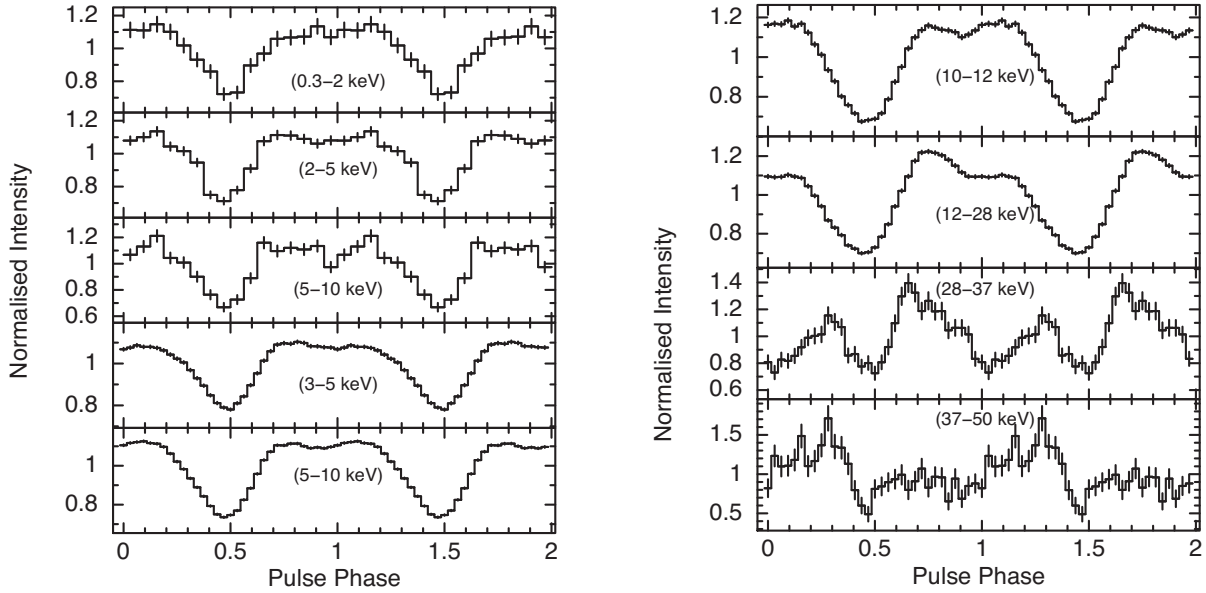
Figure 5. Energy-resolved pulse profiles of 4U 1901+03 obtained with the XRT (0.3–10 keV) and *NuSTAR* (3–79 keV) data during Obs 3.
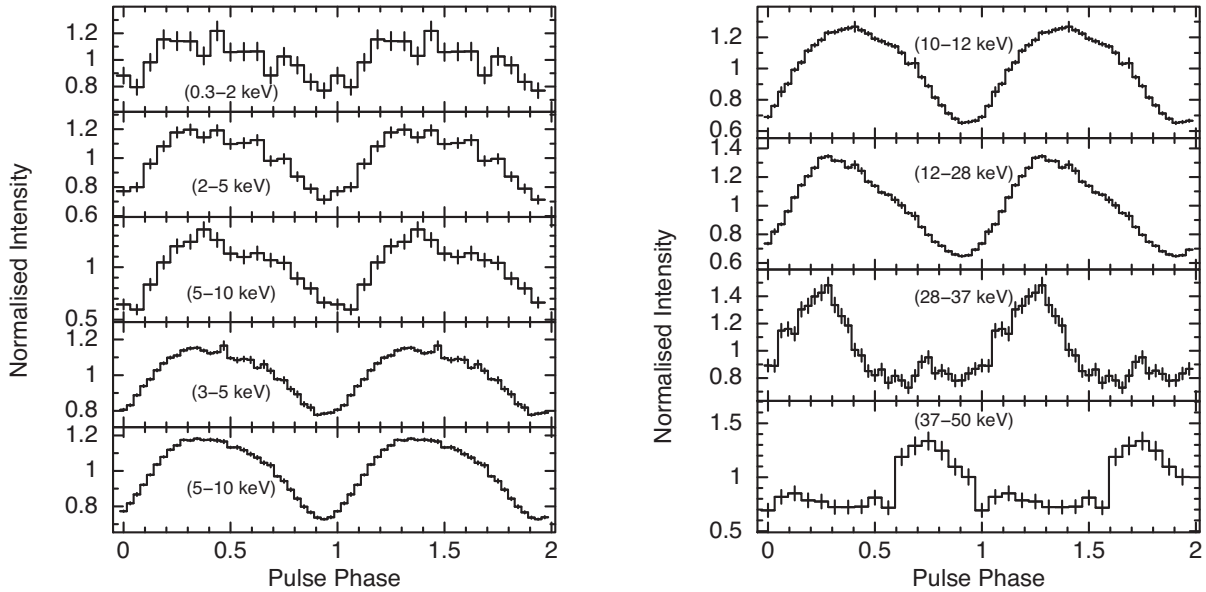

Figure 6. Energy-resolved pulse profiles of 4U 1901+03 obtained with the XRT (0.3–10 keV) and *NuSTAR* (3–79 keV) data during Obs 4.

4 SPECTRAL ANALYSIS

4.1 Phase-averaged spectral analysis

We performed X-ray spectral analysis using the combined data of *Swift*–XRT and *NuSTAR*, during all the four observations (Obs 1, 2, 3, and 4). The X-ray spectral fitting package, XSPEC (version–12.9.0; Arnaud 1996), was used. The extracted spectra were grouped to have a minimum of 25 counts per bin using the FTOOL task 'grppha'. We have used the following energy ranges for spectral fitting: 1–10 keV and 3–70 keV of XRT and NuSTAR, respectively. The XRT data below 1 keV were ignored due to spectral residuals below in the WT mode spectra.[2] To include the effects of

Galactic absorption, we have used the model component '*tbabs*' with abundances from Wilms, Allen & McCray (2000) and cross-sections as given by Verner et al. (1996). A multiplicative term (*CONSTANT*) was also added to the model to account for calibration uncertainties between the XRT and *NuSTAR*-FPMA and FPMB. The value was fixed to 1 for the *NuSTAR*-FPMA and was allowed to vary for FPMB and XRT. All fluxes were estimated using the convolution model '*CFLUX*'.

X-ray spectra of X-ray binary pulsars are thermal in nature formed in a hot plasma ($T \sim 10^8$ K) over the magnetic poles of the neutron star. The emission process is governed by the Comptonization of thermal photons, which gain energy by scattering off hot plasma electrons. Typically, shape of the X-ray spectral continuum is described by phenomenological power-law models with an exponential cutoff at higher energies (see e.g. Coburn et al. 2002a). There exist
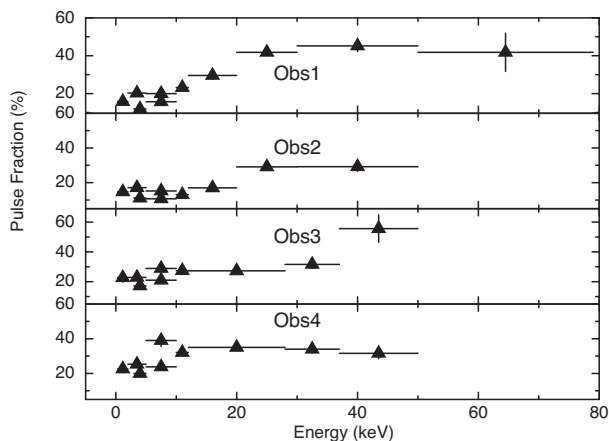
---

[2]http://www.swift.ac.uk/analysis/xrt/digest-cal.php#abs

Figure 7. This plot shows the variation of pulse fraction as a function of energy during Obs 1, 2, 3, and 4 (top to bottom). The horizontal bars on data points represent the energy ranges in which pulse fraction has been estimated whereas the vertical bars represent errors on the pulse fraction in an energy range.

several XSPEC models such as a cutoff power law ('*CUTOFFPL*'), high-energy cutoff power law ('*HIGHECUT*'), and a combination of two negative and positive power laws with exponential cutoff ('*NPEX*'). Other local models like power law with *Fermi*–Dirac cutoff ('*FDCUT*' Tanaka 1986) and a smooth high-energy cutoff model ('*NEWHCUT*' Burderi et al. 2000). We have tried all these traditional models (mentioned above) in addition to the thermal Comptonization model '*COMPTT*' (Titarchuk 1994) to fit the continuum X-ray emission of 1901 during these four observations. Adding only continuum components to the X-ray spectra of all four observations

showed the presence of a deep, broad negative residual around 10 keV. The '10 keV feature' in the *NuSTAR* spectra was also reported by Coley et al. (2019) during the 2019 outburst of 1901. Similar feature was also seen in the *RXTE* observations made during the 2003 outburst of 1901 and was interpreted as a possible cyclotron line in this source (see Reig & Milonaki 2016, for details). Therefore, we added XSPEC model *GABS*, which has three parameters: the line energy (E), width (σ), and a normalization coefficient (norm). The normalization corresponds to the line depth and is related to the optical depth, which at the line centre is given by $\tau = norm/(\sqrt{2\pi}\sigma)$. The line was centred around 10 keV ($E_{\text{Gabs\_add}}$). Adding this model component improves the fit. Furthermore, spectral residuals indicated the presence of emission features between 6 and 7 keV. Iron line emission is commonly observed in the X-ray spectra of accreting X-ray pulsars (see e.g. Basko 1978, 1980; Ebisawa et al. 1996). X-ray photons emitted from the pulsar interact with the ionized/neutral iron atoms emitting characteristic emission lines. Therefore, we added a Gaussian component centred at around 6.5 keV (*Fe K_α*). The iron line energy (E_{Fe}) did not show any significant change from Obs 1 to Obs 4. However, the equivalent width (EW) of this line was found to be variable during these observations. The maximum value of EW was observed during Obs 2. A blackbody component was also needed to fit the low-energy excess seen in all four observations. An interesting observation was the presence of negative residuals around 30 keV (E_{cyc}) in the spectral residuals of Obs 3 and Obs 4 only (see Fig. 10). Therefore, we added an another 'GABS' component to the X-ray spectra of these two observations. Addition of this component reduced the value of χ_ν^2 from 1.20 to 1.14 (2064 degrees of freedom) for Obs 3 and 1.20 to 1.14 (2064 degrees of freedom) for Obs 4. The best-fitting values obtained from the spectral fitting are given in Tables 3 and 4.
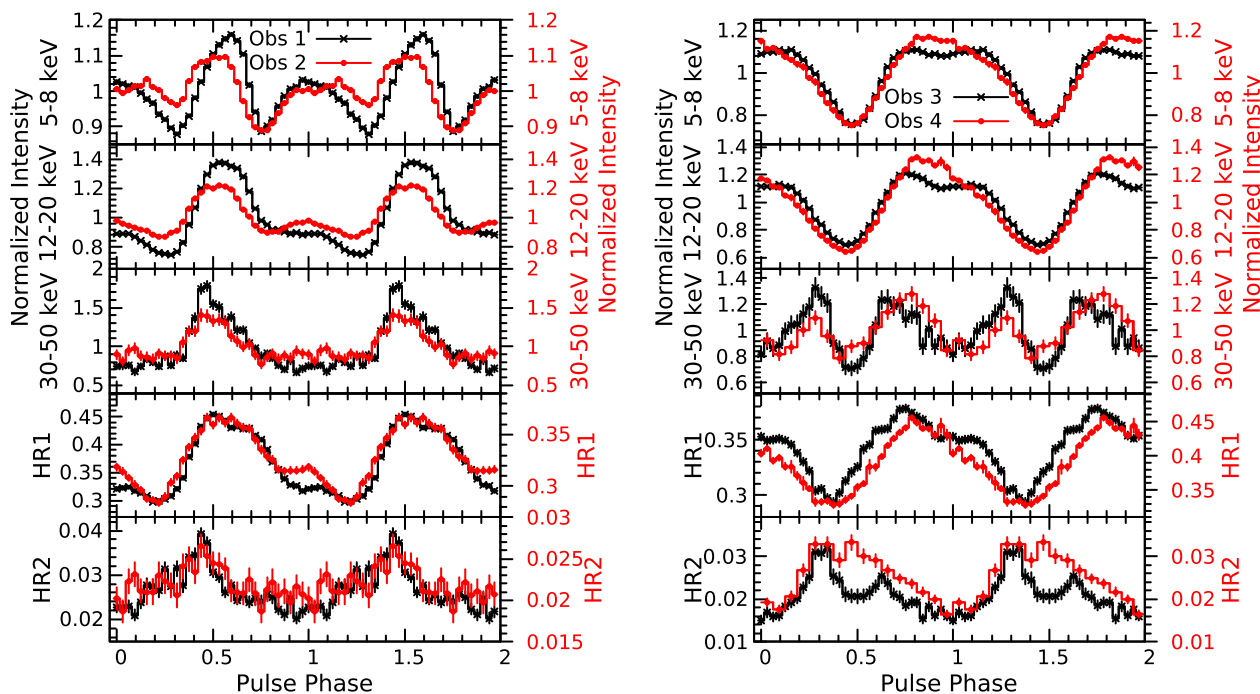
Figure 8. In the bottom two panels, we show the hardness ratio of energy-resolved pulse profiles of 4U 1901+03 obtained with *NuSTAR* data during Obs 1, 2 (left) and Obs 3, 4 (right). Top three panels of each plot show energy-resolved pulse profiles used for obtaining these hardness ratios. In the left figure, Y1 scale (left) represents data points of Obs 1 while Y2 scale (right) is for Obs 2; similarly, for figure in the right-hand side, Y1 scale represents data of Obs 3 while Y2 scale is for Obs 4. For plotting purposes, the profiles in different observations were aligned together.

Figure 9. In the left, we show hardness intensity diagram (HID) for HR1 whereas in the right plot, we show HID for HR2 (see text for details).
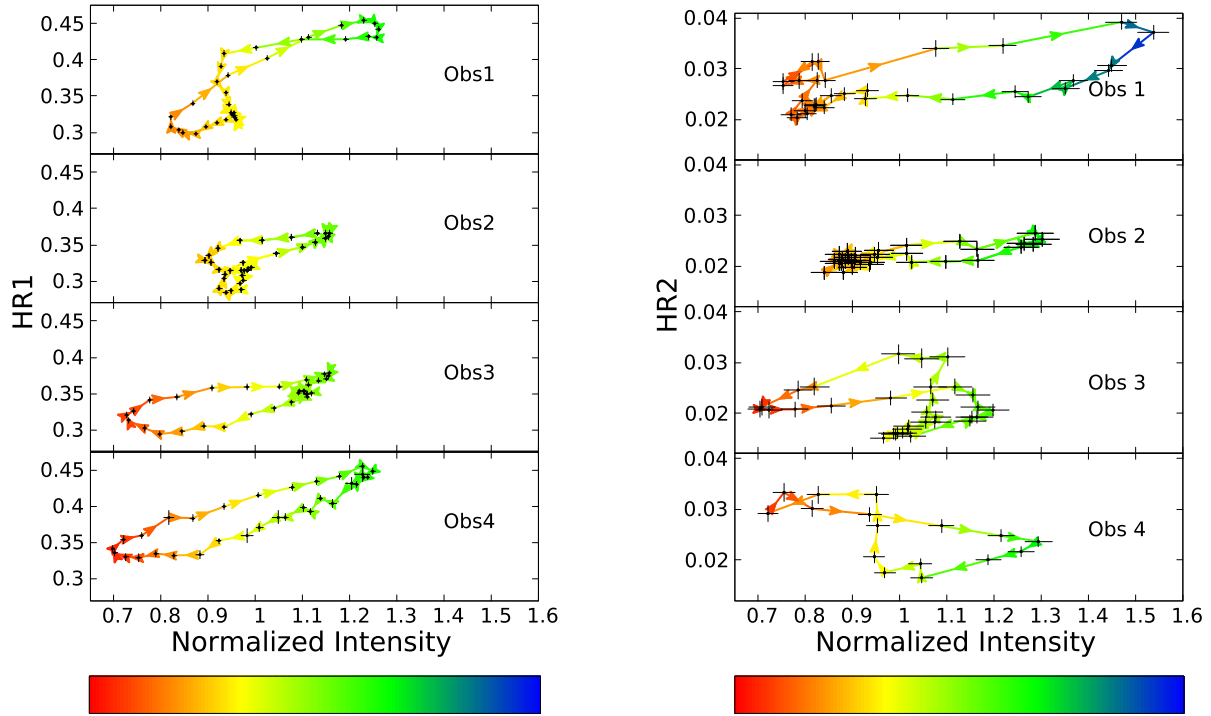
It is often observed that spectra of X-ray pulsars with high photon statistics show deviations from simple phenomenological models and a wave-like feature in the fit residuals is present between 10 and 20 keV (commonly known as '10keV feature'). The origin of this feature is still under discussion and remains unclear (see e.g. Coburn et al. 2002a; Staubert et al. 2019; Bissinger né Kühnel et al. 2020). Therefore, we attribute 30 keV feature to CRSF formed by resonant scattering of X-ray photons with electrons quantized in discrete Landau levels.

Statistical significance: To estimate significance of the detection of the CRSF at around 30 keV, we tried to fit the combined spectra of *Swift* and *NuSTAR* of Obs 3 and Obs 4 using the following model (Model 2):

const∗tbabs∗(cutoffpl∗gabs+bbodyrad+gauss+gauss), keeping its power-law index frozen to the value obtained from the best-fitting broadband spectrum. Addition of the CRSF improved the χ^2 of Obs 3 from 2439 (2067 degrees of freedom) to 2392 for 2064 degrees of freedom and for Obs 4, it changed from 2485 (2066 degrees of freedom) to 2418 (2064 degrees of freedom).

A test commonly used to infer whether the residuals with and without a model fit is systematic in nature is run-test (also called the Wald–Wolfowitz test) and is often performed to evaluate the statistical significance of a weak absorption feature against the continuum (see e.g. Orlandini et al. 2012; Maitra et al. 2017). To further verify the statistical significance of this absorption feature around 30 keV, we performed run-test (Barlow 1989) to derive the null hypothesis of the randomness in the residuals of spectral fitting in the 20–40 keV energy range. The number of data points used for the run-test in the 20–40 keV energy range is 17 (10 points below zero and 7 points above zero) for Obs 3, 22 (16 points below zero and 6 points above zero) for Obs 4. This gave the probability of obtaining $N_r \leq 3$ (where N_r is the number of runs) equals 0.06 per cent and 0.01 per cent for Obs 3 and Obs 4, respectively. These obtained values strongly indicate that the residuals are not due to random

fluctuations but have a systematic structure, and addition of CRSF component is statistically significant.

It can be seen from Tables 3 and 4 that all models (Model 1 to Model 6) provided acceptable fits to the data but Model 2 allowed us to constrain spectral-fit parameters of all the phase-resolved spectra of four observations. Therefore, we discuss in detail the results obtained with Model 2. Please note that an additional '*GABS*' component was added to all models while fitting the X-ray spectra obtained with Obs 3 and Obs 4.

The blackbody temperature measured with observations close to the peak of outburst (Obs 1 and Obs 2) was ∼0.15 keV and it decreased to ∼ 0.1 keV close to the declining phase of the outburst (Obs 3 and Obs 4). We found that photon index showed similar values (within error bars) during Obs 1, Obs 2, and Obs 3. However, a higher value (∼0.68; Model 2) was observed during Obs 4. The values of $E_{\text{Gabs\_add}}$ lie within the range of $11.4 - 8.6$ keV. E_{cyc} remained almost constant (within error bars) during Obs 3 and Obs 4.

Confidence contours were plotted to check the interdependence and to look for possible degeneracies between some of the model parameters of Obs 3. We used this observation because an additional absorption feature around 30 keV was significantly found in this and all spectral fit parameters were well constrained compared to Obs 4. Fig. 11 shows the χ^2 confidence contours between pairs of some of the model parameters. It can be seen that photon index (Γ) and cutoff energy (E_{cut}) are correlated and difficult to constrain independently while $E_{\text{Gabs\_add}}$ at 10 keV and cutoff energy (E_{cut}) could be well constrained.

4.2 Phase-resolved spectroscopy

Motivated by the change in HR as indicated by Fig. 8, we performed a spin phase-resolved spectroscopy to understand the accretion geometry and surrounding of the pulsar. We accumulated the
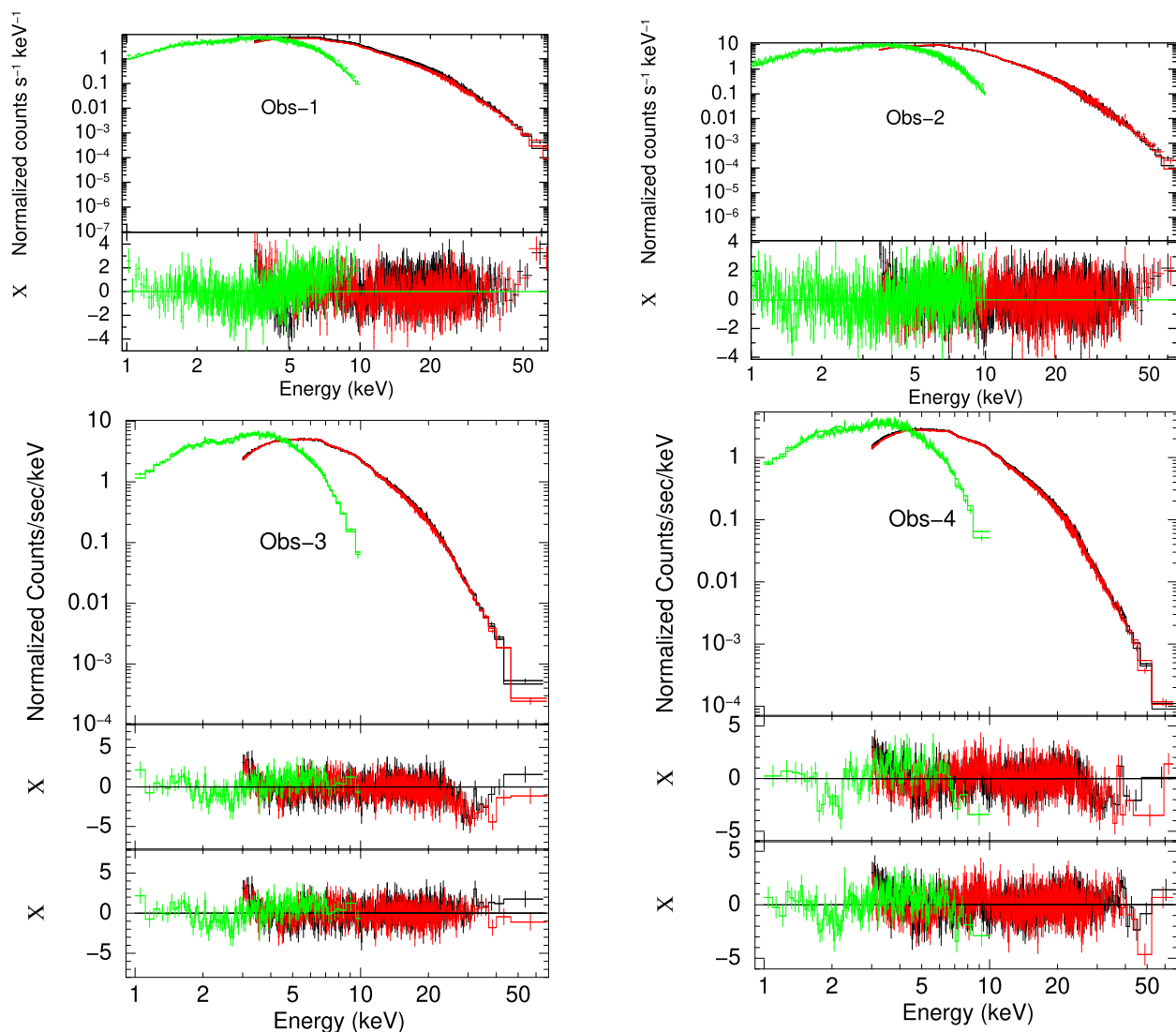
Figure 10. Phase-averaged spectra obtained with *Swift*-XRT and *NuSTAR* during four observations made during 2019 outburst of 1901. The residuals in the middle panel of bottom two plots indicate the presence of a cyclotron resonance scattering feature (CRSF). The plot has been created using Model 2 spectral fit parameters.

phase-sliced spectra in 10 phase bins using the XSELECT package. It is worth mentioning that while performing phase-resolved spectroscopy, we have used only the *NuSTAR* (FPMA and FPMB) data as *Swift* observations were not strictly simultaneous. We have used the same response matrices and effective area files as used for phase-averaged spectroscopy. Spectral studies were carried out in the 3–70 keV energy range using the same technique as opted while performing phase-averaged spectroscopy. For all four observations, we fixed iron line widths and neutral hydrogen column density to the best-fitting values obtained for the phase-averaged spectroscopy. We observed that for Obs 1, the addition of a blackbody component was needed to obtain the best fit while it was not included for rest of the observations. In the case of Obs 3 and Obs 4, we also fixed width (σ_{cyc}) of the E_{cyc} to the best-fitting phase-averaged values as it was difficult to constrain these while performing phase-resolved spectroscopy.

Figs 12 and 13 show spectral parameters obtained from the phase-resolved spectroscopy. The top two panels in these plots show the pulse profiles in 3–10 keV and 10–70 keV energy bands. The

bottom two panels show corresponding values of the source flux. In Fig. 12 (left), continuum spectral parameters such as blackbody temperature (kT), photon index (Γ), and high energy cut (E_{cut}) are shown in the third, fourth, and fifth panels, respectively. As mentioned earlier, blackbody component was not required for Obs 2, 3, and 4; therefore, we show Γ and E_{cut} in the third and fourth panels, respectively, for these observations (see right plot of Figs 12 and 13). It can be clearly seen that all these parameters significantly vary over pulse phase. Γ and E_{cut} were found to be strongly correlated and might indicate degeneracy between the two model parameters. This is consistent with that observed from the confidence contours between these two parameters (Fig. 11). The blackbody temperature showed a variation between 0.1 and 0.5 keV and an anticorrelation was observed between photon index and blackbody temperature for Obs 1. Photon index varied between 0.2 and 1 during Obs 1 while it showed values between 0.6 and 0.85 during Obs 2. During all observations, we observed a low value of Γ during peak of the pulse profiles, indicating that spectra are harder during these phases. This is well consistent with the previous reports of this source
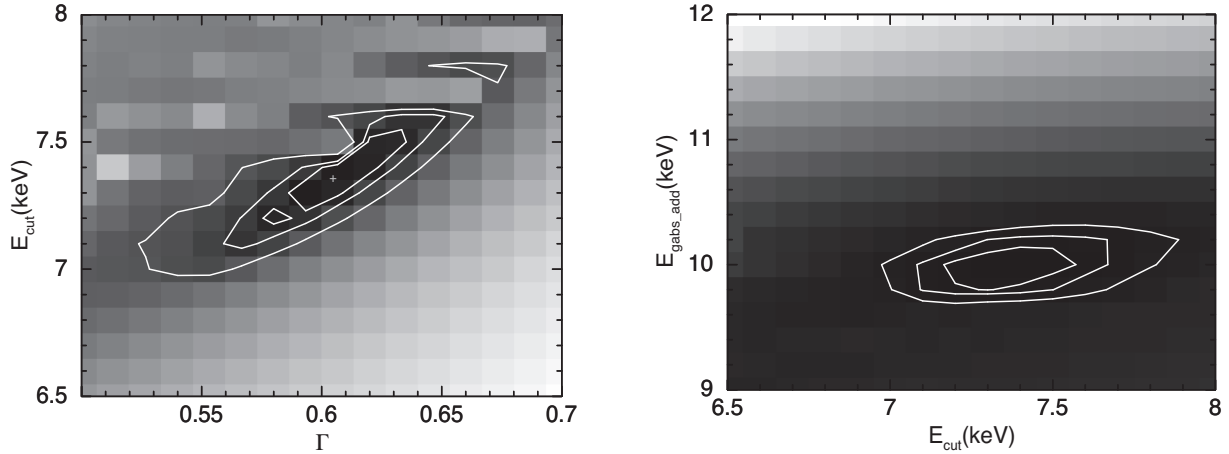
Figure 11. χ^2 confidence contours between photon index (Γ) and cutoff energy (E_{cut}) on the left while on the right, we show confidence contours between E_{cut} and $E_{\mathrm{Gabs\_add}}$ at 10 keV, obtained from the phase-averaged spectra of Obs 3. The innermost to outermost contours represent, respectively, 68 per cent, 90 per cent, and 99 per cent confidence levels.

and also typical of X-ray pulsars. Iron line energy (E_{Fe}) did not show any variation across the pulse phase; however, we observe some anticorrelation between its equivalent width (EW_{Fe}) and pulse profiles. A clear correlation could be seen between E_{cut} and $E_{\mathrm{Gabs\_add}}$ in all observations. '10 keV feature' showed variation across pulse phase in all four observations. For Obs 1, 2, and 3, line centroid energy varied between 9 and 11 keV while for Obs 4, it showed a value between 7 and 10 keV. There also exist some correlation between $\tau_{\mathrm{Gabs_{add}}}$ and pulse profiles. E_{cyc} varies by ~ 60 per cent (22–42 keV) and ~ 47 per cent (29–44 keV) for Obs 3 and Obs 4, respectively, and there exist a correlation between pulse profiles (shown in top panels of Fig. 13) and E_{cyc}. Moreover, τ_{cyc} also showed variation across the pulse phase with a trend similar to that observed in the pulse profiles of 28–37 keV band (see Fig. 14).

The 30-keV absorption feature was not detected in the phase-averaged spectra of Obs 1 and Obs 2. In order to probe the presence of this feature, we looked carefully at the pulse phase-resolved spectra of these observations. Consequently, for Obs 1, we found dip-like structures at around 30 keV, 38 keV, and 29 keV in the spectral residuals of the following three pulse phases: 0.0–0.1, 0.8–0.9, and 0.9–1.0, respectively. This feature did not appear in the rest of the pulse phases. Similarly, for Obs 2, we found the presence of E_{cyc} at around 38 keV in the phase-resolved spectra at 0.0–0.1, 0.1–0.2 pulse phase, 34 keV for the spectrum at 0.2–0.3 pulse phase, and 40 keV for 0.9–1.0 pulse phase (Fig. 15). These values of E_{cyc} are consistent with those observed for Obs 3 and Obs 4. Therefore, an additional '*GABS*' component was added to the X-ray spectra of these observations. We computed the statistical significance of detection of the CRSF using the run-test as opted for phase-averaged spectra of Obs 3 and Obs 4 (refer to Section 4.1 for details). The values mentioned in Table 2 and the residuals in Fig. 15 show that the detection of the CRSF in the X-ray spectra at certain pulse phases is significant. The variation of E_{cyc} parameters with the pulse phase is shown in Fig. 12. During Obs 1, E_{cyc} was observed during the off-peak pulse phases, whereas during Obs 2, the CRSF was detected during the pulse peaks. τ_{cyc} showed a trend similar to that observed for E_{cyc} during both observations. The values of X-ray flux across pulse phases where the CRSF has been detected were compared to those measured during phases where there is no detection. Thus, presence/absence of CRSF did not show a clear dependence on the X-ray flux.

5 DISCUSSION

In this work, we have performed a detailed broadband timing and spectral analysis with *Swift* and *NuSTAR*. We discuss our results as follows:

5.1 Timing results

5.1.1 Pulse profile evolution with the X-ray luminosity

As can be seen from Fig. 1 that *NuSTAR* and *Swift* observations were taken at different levels of intensity and, therefore, we calculated the values of X-ray luminosity (L_{X}) during these observations (Obs 1, 2, 3, and 4), assuming source distance to be 3 kpc. We have used the values of X-ray flux obtained in the 1–70 keV band during these observations (refer to Tables 3 and 4) and found L_{X} to be $\sim 0.76 \times 10^{37}\,\mathrm{ergs\,s^{-1}}$, $0.85 \times 10^{37}\,\mathrm{ergs\,s^{-1}}$, $0.5 \times 10^{37}\,\mathrm{ergs\,s^{-1}}$, and $0.3 \times 10^{37}\,\mathrm{ergs\,s^{-1}}$ for Obs 1, 2, 3, and 4, respectively. Thus, these observations allowed us to probe into luminosity dependence of pulse profiles. We found that pulse profiles show a strong evolution with the change in L_{X} (see Fig. 2).

Due to effect of the non-spherical emission region and scattering cross-sections of the photons, which are altered in the presence of strong magnetic fields, different beaming patterns of radiation, 'Fan' or 'Pencil', are produced depending on the mass accretion rate on the neutron star (Nagel 1981; Meszaros & Nagel 1985). The critical luminosity (L_{crit}) indicates whether the radiation pressure of the emitting plasma is capable of decelerating the accretion flow and plays a role in defining two accretion regimes. If the L_{X} is greater than L_{crit} (supercritical regime), then radiation pressure is high enough to stop the accreting matter at a distance above the neutron star, forming a radiation-dominated shock (Fan beam). If L_{X} is less than L_{crit}, then the accreted material reaches the neutron star surface through coulomb collisions with thermal electrons or through nuclear collisions with atmospheric protons (Pencil beam) (Harding 1994). However, it has been found/proposed that beaming patterns can be much more complex than a simple pencil/fan beam (Kraus et al. 1995, 1996; Becker et al. 2012; Mushtukov et al. 2015a) and accretion regimes can also be probed by observing changes in the pulse profiles, cyclotron line energies, and changes in the spectral shape (see e.g. Parmar et al. 1989; Reig & Nespoli 2013;
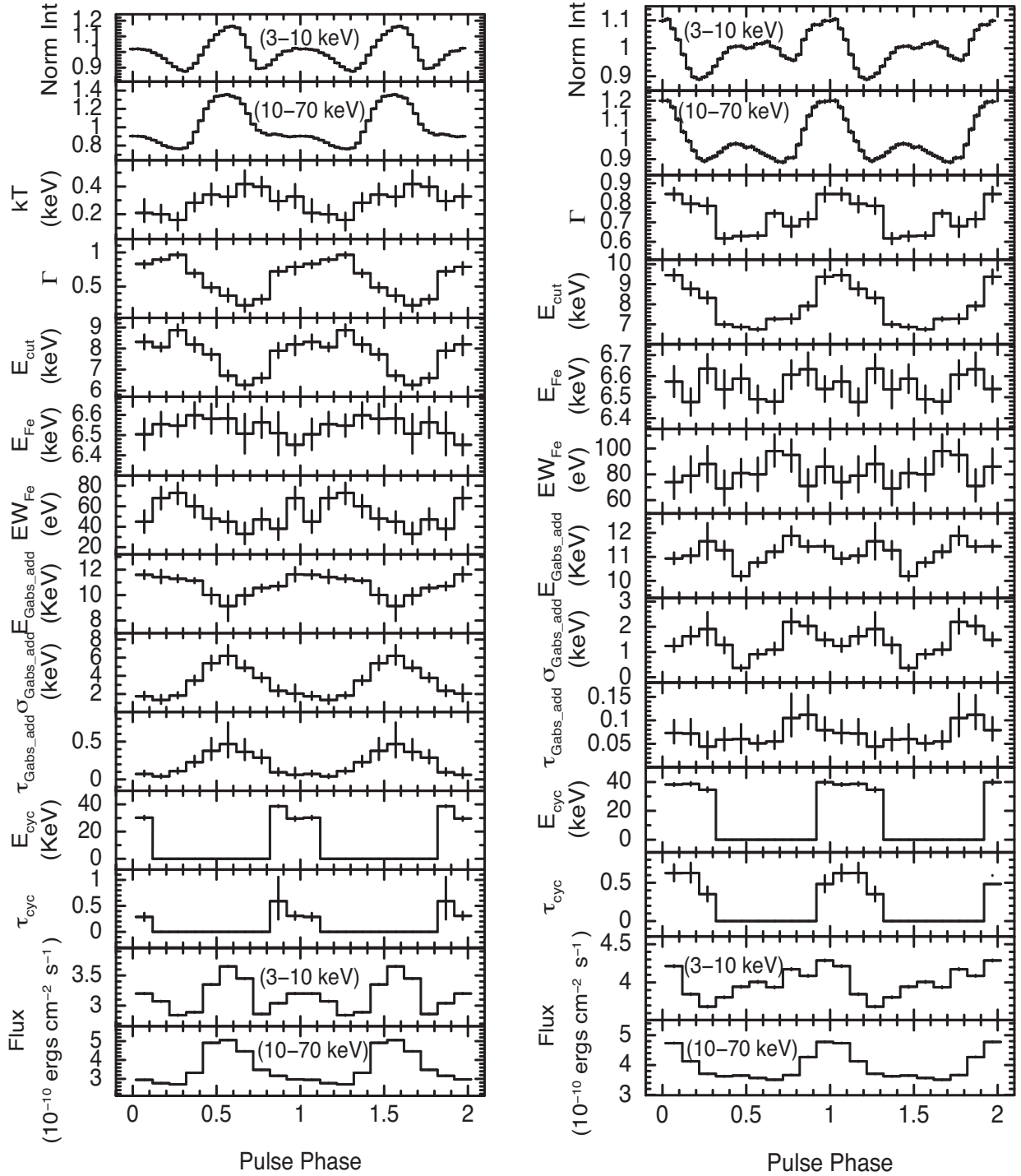
Figure 12. This plot shows variation of spectral parameters across the pulse phase for Obs 1 (left) and Obs 2 (right). We have used Model 2 for performing phase-resolved spectroscopy (please see text for details). Here, we would like to mention that the value 0 in E_{cyc} and τ_{cyc} panels corresponds to observations, which did not require this component for obtaining the best fit.

Mushtukov et al. 2015a). Observations made with *NICER* and *Insight-HXMT* revealed the value of critical luminosity in this source to be $\sim 1 \times 10^{37}$ ergs s^{-1} (Ji et al. 2020; Tuo et al. 2020). Thus, observations used in our work were taken below the critical luminosity or belong to sub-critical regime.

From Fig. 2, we found a strong luminosity dependence of the pulse profiles of 1901. A secondary peak (or notch) could be

clearly seen in the pulse profiles of Obs 1 and Obs 2 (except *Swift* pulse profiles) while the pulse profiles during Obs 3 and Obs 4 were simple, broad, and single-peaked. Ji et al. (2020) found that close to 0.8×10^{37} ergs s^{-1}, the notch (or secondary peak) appears in the pulse profiles, whereas below 0.7×10^{37} ergs s^{-1} pulse profiles are single peaked. Thus, our results are consistent with that obtained by Ji et al. (2020) and similar pulse profiles
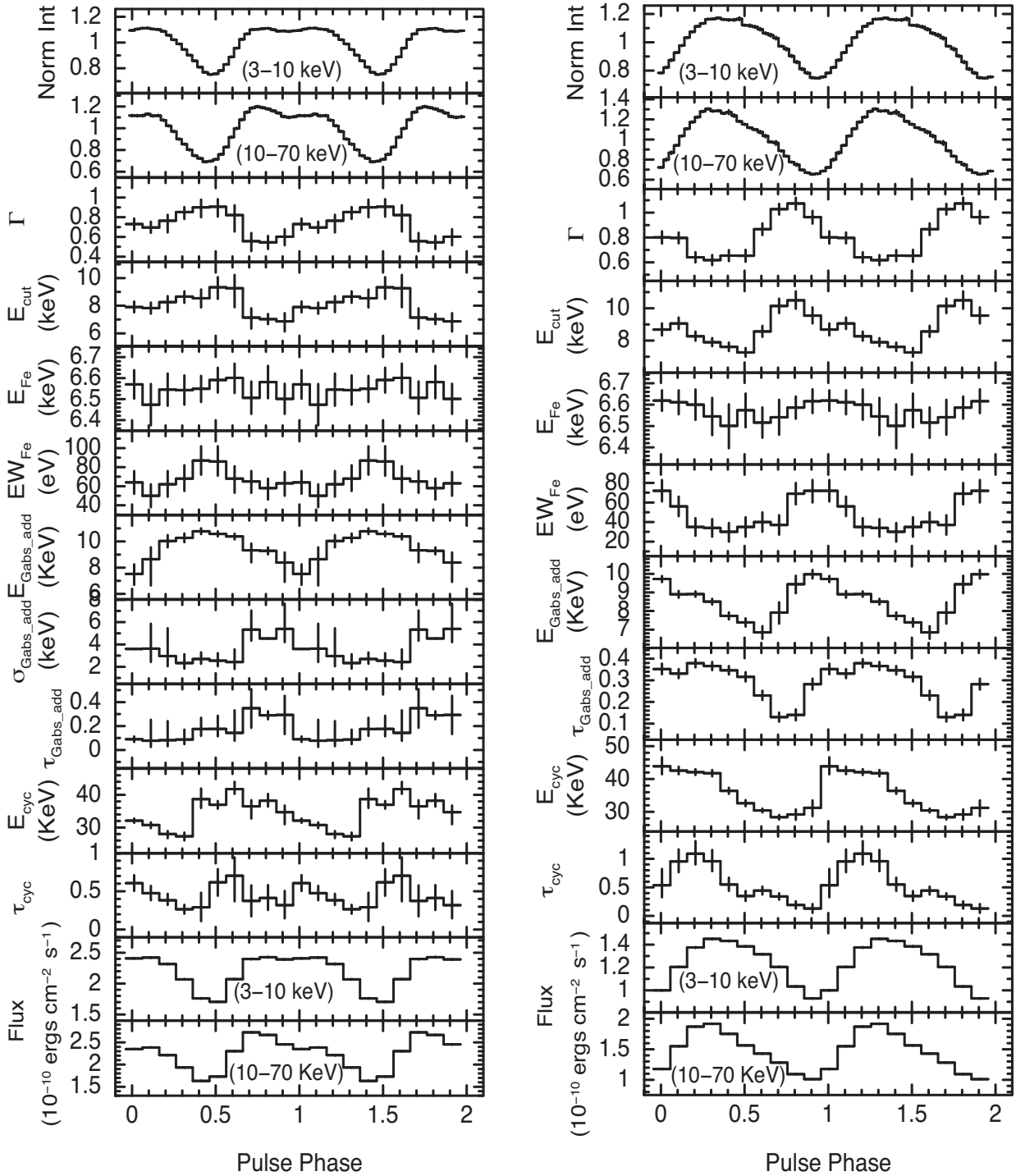
Figure 13. This plot shows variation of spectral parameters across the pulse phase for Obs 3 (left) and Obs 4 (right). Model 2 was used for performing phase-resolved spectroscopy.

were also seen during the 2003 outburst of 1901 (see e.g. Chen et al. 2008; Reig & Milonaki 2016). Based on a detailed study of pulse profiles of 1901 using the *NICER* and *Insight-HXMT* data, Ji et al. (2020) proposed that pulse profiles of 1901 show a complex luminosity dependence and can be formed with a combination of 'fan' and 'pencil' beams. Fan beam dominating the high-luminosity observations while pencil beam at low luminosity (see also Chen et al. 2008).

5.1.2 Energy dependence of pulse profiles: an abrupt change close to the CRSF

A strong energy dependence of pulse profiles has been observed in several X-ray pulsars like 4U 0115+63 (Tsygankov et al. 2007), 4U 1626–67 (see e.g. Beri et al. 2014), LMC X–4 (see e.g. Beri & Paul 2017), and 1A 1118-61 (e.g. Maitra et al. 2012). It is usually found that pulse profiles tend to be simpler at higher energies (above
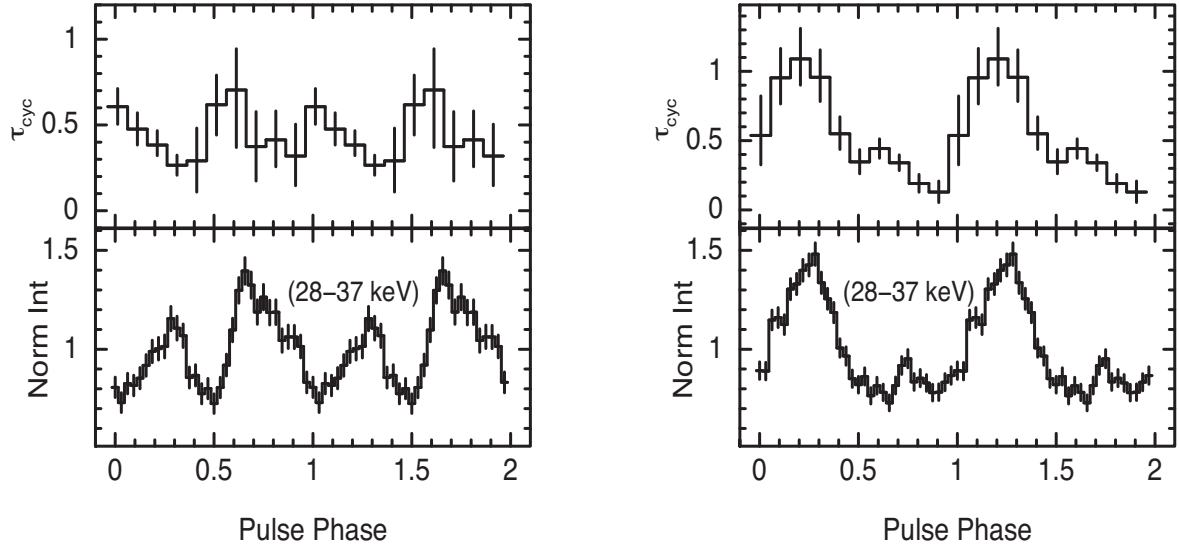
Figure 14. This plot shows a similarity between the optical depth (τ_{cyc}) and pulse profile in the 28–37 keV energy band for Obs 3 (left) and Obs 4 (right).
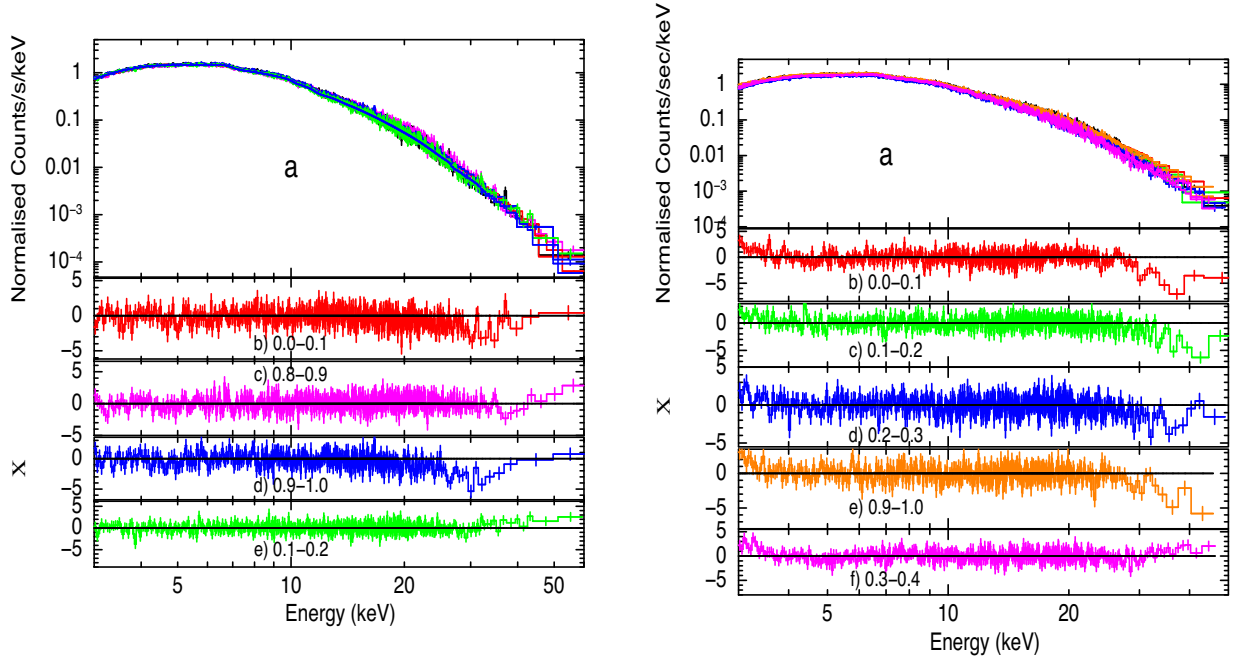

Figure 15. a. We show phase-resolved spectra of 4U 1901+03 during Obs 1 (left) and Obs 2 (right). For clarity, we have included data only from FPMA. Panels (b, c, and d) in the left show residuals from the best-fitting phase-resolved spectra of 4U 1901+03, obtained using Model 2 without additional absorption component at 30 keV and for comparison, we show residuals of the phase-resolved spectrum where no negative residuals around 30 keV were observed (bottom panel, e). Similarly, in the right, panels (b, c, d, and e) indicate negative residuals around E_{cyc} while the bottom panel (f) are residuals across the pulse phase where 30 keV feature was not seen.

10 keV) compared to complex profiles observed at lower energies (see e.g. Devasia et al. 2011). A similar energy dependence of the pulse profiles was found during Obs 1 and Obs 2 (see Figs 3 and 4). However, it was interesting to note that during Obs 3, energy-resolved pulse profiles showed a change in the general trend. They changed from simple, broad to complex pulse profiles above 28 keV. Two prominent peaks with a dip at around pulse phase 0.5 appeared in the pulse profiles of 28–37 keV energy band (see Fig. 5). Obs 4 also showed similar features in the pulse profile of this energy band. Based on the relationship proposed by Mushtukov et al. (2015b) between the critical luminosity and magnetic field

of neutron star, Ji et al. (2020) suggested 30 keV to be energy of the CRSF in 1901. Scattering cross-sections are believed to be significantly modified and increase by a large factor near the CRSF (Araya & Harding 1999; Araya-Góchez & Harding 2000; Schönherr et al. 2007), causing a change in the beaming patterns. There also exist several reports where significant changes in the shape of pulse profiles have been found near the cyclotron line energies [see e.g. V 0332+53 (Tsygankov et al. 2006) and 4U 0115+63 (Ferrigno et al. 2011)]. Thus, it may be possible that the abrupt change observed in the pulse profiles around 30 keV is due to the existence of cyclotron line of this system at around this energy. Such prominent changes

Table 2. Table shows the values of probability of chance improvement (PCI) obtained on performing the run-test on residuals of the phase-resolved X-ray spectra of Obs 1 and Obs 2. PCI corresponds to $N_r < =3$ (number of runs), N_+ (points above zero), and N_- (points below zero).

	Obs 1		
Pulse phase	PCI	N_+	N_-
0.0–0.1	0.3 %	6	8
0.8–0.9	0.05%	7	11
0.9–1.0	0.02%	16	5
	Obs 2		
Pulse phase	PCI	N_+	N_-
0.0–0.1	0.09%	9	7
0.1–0.2	0.03%	9	9
0.2–0.3	0.04%	3	22
0.9–1.0	0.5%	2	21

in the pulse profiles were seen only in observations made during declining phase of the outburst (Obs 3 and Obs 4); this further suggest a strong luminosity dependence of the beaming pattern.

Pulse fraction that quantifies the fraction of X-ray photons contributing to the observed pulsation showed an increase with the increasing energy, suggesting large contribution from the hard X-rays. Similar dependence on energy has also been observed in several X-ray pulsars (Nagase 1989; Bildsten et al. 1997).

5.2 Spectral results

5.2.1 L_X dependence: continuum parameters, 10 keV feature and iron line

Our spectral results indicated the presence of hard X-ray spectrum, which is typical of X-ray pulsars. The values of Γ found are consistent with that observed during its previous outburst in 2003

Table 3. Spectral fit parameters with other phenomenological models. We have performed spectral fitting in the 1–79 keV band.

Parameters	Model 1	Model 2	Model 3	Model 4	Model 5	Model 6
			Observation 1			
N_H (10^{22}cm^{-2})	4.5 ± 0.2	5.6 ± 0.2	6.2 ± 0.3	5.3 ± 0.2	7.2 ± 0.3	8.9 ± 0.2
Γ	0.55 ± 0.02	0.60 ± 0.02	0.53 ± 0.03	0.58 ± 0.02	1.3 ± 0.1	–
$E_{cut/break/e}$ (keV)	3.65 ± 0.07	7.6 ± 0.1	4.73 ± 0.04	1.7 ± 0.2	10 ± 2	–
E_{fold} (keV)	7.5 ± 0.1	–	–	7.5 ± 0.1	8.4 ± 0.1	–
kT_{bb} (keV)	0.17 ± 0.02	0.15 ± 0.01	0.15 ± 0.01	0.15 ± 0.01	0.14 ± 0.01	0.131 ± 0.005
kT_e (keV)	–	–	–	–	–	4.94 ± 0.03
τ	–	–	–	–	–	4.92 ± 0.04
N^a	0.21 ± 0.01	0.39 ± 0.01	0.46 ± 0.02	0.29 ± 0.02	0.92 ± 0.04	–
E_{Fe} (keV)	6.52 ± 0.03	6.52 ± 0.03	6.50 ± 0.03	6.52 ± 0.03	6.51 ± 0.03	6.6 ± 0.1
EW_{Fe} (eV)	57 ± 7	48 ± 6	50 ± 7	52 ± 8	49 ± 7	20 ± 3
E_{Gabs_add} (keV)	10.8 ± 0.1	10.7 ± 0.1	10.8 ± 0.2	10.7 ± 0.1	11.3 ± 0.1	11.3 ± 0.3
σ_{Gabs_add} (keV)	3.4 ± 0.3	3.6 ± 0.3	1.5 ± 0.2	3.8 ± 0.3	0.9 ± 0.2	1.69 ± 0.04
τ_{Gabs_add}	0.16 ± 0.05	0.17 ± 0.05	0.15 ± 0.04	0.17 ± 0.05	0.22 ± 0.03	0.08 ± 0.03
const$_{FPMB}$	0.978 ± 0.002	0.978 ± 0.002	0.978 ± 0.002	0.978 ± 0.002	0.978 ± 0.002	0.978 ± 0.002
const$_{XRT}$	0.99 ± 0.01	0.99 ± 0.01	0.99 ± 0.01	0.99 ± 0.01	1.00 ± 0.01	0.99 ± 0.01
Unabsorbed flux(1–79 keV)^b	7.1 ± 0.1	7.1 ± 0.1	7.1 ± 0.1	7.1 ± 0.1	7.1 ± 0.1	7.1 ± 0.1
Reduced χ^2 (degrees of freedom)	1.24 (2223)	1.28 (2224)	1.27 (2221)	1.27 (2221)	1.27 (2221)	1.31 (2222)
			Observation 2			
N_H (10^{22}cm^{-2})	4.3 ± 0.3	5.7 ± 0.2	5.2 ± 0.2	5.3 ± 0.3	6.4 ± 0.2	1.82 ± 0.07
Γ	0.51 ± 0.03	0.56 ± 0.02	0.41 ± 0.06	0.55 ± 0.03	0.93 ± 0.03	–
$E_{cut/break/e}$ (keV)	3.8 ± 0.1	7.1 ± 0.1	6.2 ± 0.3	1.9 ± 0.5	1^c	–
E_{fold} (keV)	6.9 ± 0.1	–	–	$6.97^{+0.09}_{-0.07}$	7.5 ± 0.1	–
kT_{bb} (keV)	0.18 ± 0.01	0.15 ± 0.01	0.15 ± 0.01	0.16 ± 0.01	0.15 ± 0.01	–
kT_e (keV)	–	–	–	–	–	4.69 ± 0.04
τ	–	–	–	–	–	4.85 ± 0.04
N^a	0.23 ± 0.01	0.44 ± 0.01	0.37 ± 0.02	0.32 ± 0.02	1.07 ± 0.04	–
E_{Fe} (keV)	6.50 ± 0.03	6.53 ± 0.03	6.52 ± 0.03	6.53 ± 0.03	6.55 ± 0.04	6.53 ± 0.03
EW_{Fe} (eV)	97 ± 10	75 ± 8	66 ± 7	80 ± 9	98 ± 9	75 ± 9
E_{Gabs_add} (keV)	11.4 ± 0.1	11.4 ± 0.1	11.3 ± 0.1	11.4 ± 0.1	11.6 ± 0.1	10.7 ± 0.3
σ_{Gabs_add} (keV)	1.9 ± 0.2	1.9 ± 0.2	2.2 ± 0.2	1.9 ± 0.2	1.8 ± 0.2	1.4 ± 0.2
τ_{Gabs_add}	0.09 ± 0.01	0.09 ± 0.01	0.11 ± 0.02	0.09 ± 0.01	0.09 ± 0.01	0.04 ± 0.01
const$_{FPMB}$	1.080 ± 0.003	1.081 ± 0.003	1.080 ± 0.003	1.080 ± 0.003	1.080 ± 0.003	1.080 ± 0.003
const$_{XRT}$	$1.048^{+0.009}_{-0.008}$	1.04 ± 0.01	$1.040^{+0.009}_{-0.008}$	1.04 ± 0.01	1.041 ± 0.007	1.044 ± 0.008
Unabsorbed flux (1–79 keV)^b	8.0 ± 0.2	8.1 ± 0.1	8.1 ± 0.2	8.1 ± 0.2	8.0 ± 0.2	8.0 ± 0.2
Reduced χ^2 (degrees of freedom)	1.12 (2140)	1.14 (2141)	1.13 (2140)	1.14 (2140)	1.17 (2141)	1.18 (2142)

^{a}Normalization (N) is in units of photons cm^{-2} s^{-1} keV^{-1} at 1 keV.
^{b}Unabsorbed flux in units 10^{-9}ergs cm^{-2}s^{-1}.
^{c}Fixed parameters.
Model 1: const∗tbabs∗(powerlaw∗highecut∗gabs+bbodyrad+gauss).
Model 2: const∗tbabs∗(cutoffpl∗gabs+bbodyrad+gauss).
Model 3: const∗tbabs∗(NPEX∗gabs+bbodyrad+gauss).
Model 4: const∗tbabs∗(powerlaw∗newhcut∗gabs+bbodyrad+gauss).
Model 5: const∗tbabs∗(powerlaw∗fdcut∗gabs+bbodyrad+gauss).
Model 6: const∗tbabs∗(comptt∗gabs+bbodyrad+gauss).

Table 4. Spectral fit parameters obtained for Observations 3 and 4.

Parameters	Model 1	Model 2	Model 3	Model 4	Model 5	Model 6
			Observation 3			
N_H (10^{22} cm^{-2})	3.4 ± 0.1	4.4 ± 0.2	3.8 ± 0.1	3.9 ± 0.2	5.6 ± 0.3	6.7 ± 0.2
Γ	0.55 ± 0.02	0.61 ± 0.04	0.46 ± 0.05	0.56 ± 0.04	1.3 ± 0.1	–
$E_{cut/break/e}$ (keV)	3.2 ± 0.1	7.4 ± 0.2	4.8 ± 0.1	1.1 ± 0.3	11 ± 2	–
E_{fold} (keV)	7.2 ± 0.1	–	–	$7.44^{+0.16}_{-0.22}$	8.0 ± 0.2	–
kT_{bb} (keV)	0.08 ± 0.02	0.10 ± 0.02	$0.12^{+0.01}_{-0.02}$	0.10 ± 0.02	0.12 ± 0.01	0.12 ± 0.01
kT_e (keV)	–	–	–	–	–	5.0 ± 0.1
τ	–	–	–	–	–	5.1 ± 0.1
N[a]	0.158 ± 0.005	0.28 ± 0.01	0.27 ± 0.02	0.23 ± 0.01	0.63 ± 0.03	–
E_{Fe} (keV)	6.54 ± 0.03	6.54 ± 0.03	6.53 ± 0.03	6.55 ± 0.03	6.52 ± 0.04	6.45 ± 0.05
EW_{Fe} (eV)	64 ± 9	64 ± 9	58 ± 8	64 ± 8	61 ± 8	116 ± 16
E_{Gabs_add} (keV)	10.2 ± 0.2	9.9 ± 0.2	10.4 ± 0.1	10.0 ± 0.2	10.9 ± 0.1	11.5 ± 0.2
σ_{Gabs_add} (keV)	3.2 ± 0.3	3.7 ± 0.4	2.3 ± 0.3	3.6 ± 0.4	1.9 ± 0.3	1.7 ± 0.3
τ_{Gabs_add}	0.17 ± 0.02	0.18 ± 0.04	0.08 ± 0.01	0.18 ± 0.02	0.07 ± 0.02	0.07 ± 0.01
E_{cyc} (keV)	32.4 ± 0.7	33 ± 2	33 ± 1	33 ± 2	32 ± 1	34 ± 1
σ_{cyc} (keV)	4.8 ± 0.5	6 ± 1	7.0 ± 2.0	5 ± 1	5 ± 1	9.96[c]
τ_{cyc}	0.21 ± 0.06	0.23 ± 0.08	0.4 ± 0.1	0.23 ± 0.09	0.23 ± 0.09	0.48 ± 0.07
$const_{FPMB}$	1.052 ± 0.003	1.052 ± 0.003	1.052 ± 0.003	1.052 ± 0.003	1.052 ± 0.003	1.052 ± 0.003
$const_{XRT}$	1.15 ± 0.01	1.15 ± 0.01	1.15 ± 0.01	1.15 ± 0.01	1.15 ± 0.01	1.16 ± 0.01
Unabsorbed flux (1–79 keV)[b]	4.7 ± 0.1	4.7 ± 0.1	4.7 ± 0.1	4.7 ± 0.1	4.7 ± 0.1	4.7 ± 0.1
Reduced χ^2 (degrees of freedom)	1.10 (2064)	1.14 (2064)	1.16 (2064)	1.14 (2063)	1.12 (2063)	1.14 (2065)
			Observation 4			
N_H (10^{22} cm^{-2})	3.1 ± 0.1	3.7 ± 0.1	4.8 ± 0.2	3.3 ± 0.2	5.1 ± 0.2	5.5 ± 0.2
Γ	0.62 ± 0.03	0.68 ± 0.02	0.87 ± 0.02	0.63 ± 0.02	1.44 ± 0.05	–
$E_{cut/break/e}$ (keV)	3.1 ± 0.1	7.9 ± 0.1	4.63 ± 0.05	1.2 ± 0.3	17 ± 2	–
E_{fold} (keV)	7.6 ± 0.1	–	–	7.6 ± 0.1	7.7 ± 0.1	–
kT_{bb} (keV)	0.08 ± 0.02	0.08 ± 0.02	0.10 ± 0.01	0.09 ± 0.01	0.10 ± 0.01	0.10 ± 0.01
kT_e (keV)	–	–	–	–	–	4.94 ± 0.06
τ	–	–	–	–	–	5.18 ± 0.06
N[a]	0.13 ± 0.02	0.19 ± 0.01	0.30 ± 0.01	0.14 ± 0.02	0.38 ± 0.02	–
E_{Fe} (keV)	6.57 ± 0.03	6.58 ± 0.03	6.54 ± 0.03	6.54 ± 0.03	6.56 ± 0.03	6.55 ± 0.03
EW_{Fe} (eV)	43 ± 6	42 ± 6	51 ± 6	41^{+17}_{-30}	46 ± 7	44 ± 6
E_{Gabs_add} (keV)	8.8 ± 0.1	8.6 ± 0.1	11.2 ± 0.6	9.1 ± 0.3	9.1 ± 0.3	10.2 ± 0.3
σ_{Gabs_add} (keV)	4[c]	4[c]	1.3 ± 0.6	4[c]	5 ± 1	3.6 ± 0.5
τ_{Gabs_add}	0.29 ± 0.02	0.29 ± 0.02	0.02 ± 0.02	0.28 ± 0.02	0.13 ± 0.02	0.09 ± 0.03
E_{cyc} (keV)	32.6 ± 0.8	35 ± 1	31.7 ± 0.6	32 ± 1	30 ± 1	32 ± 1
σ_{cyc} (keV)	3.45[c]	4.44[c]	6.73[c]	3.5[c]	4.12[c]	5.54[c]
τ_{cyc}	0.14 ± 0.03	0.18 ± 0.03	0.31 ± 0.04	0.12 ± 0.03	0.16 ± 0.03	0.23 ± 0.02
$const_{FPMB}$	1.025 ± 0.002	1.025 ± 0.002	1.025 ± 0.002	1.025 ± 0.002	1.025 ± 0.002	1.025 ± 0.002
$const_{XRT}$	0.94 ± 0.01	0.94 ± 0.01	0.94 ± 0.01	0.94 ± 0.01	0.94 ± 0.01	0.94 ± 0.01
Unabsorbed flux (1–79 keV)[b]	2.9 ± 0.1	2.9 ± 0.1	2.9 ± 0.1	2.9 ± 0.1	2.9 ± 0.1	2.9 ± 0.1
Reduced χ^2 (degrees of freedom)	1.13 (2064)	1.17 (2065)	1.09 (2063)	1.17 (2064)	1.09 (2064)	1.08 (2064)

[a]Normalization (N) is in units of photons cm^{-2} s^{-1} keV^{-1} at 1 keV.

[b]Unabsorbed flux in units 10^{-9} ergs cm^{-2} s^{-1}.

[c]Fixed parameters.

(see fig. 4 of Reig & Milonaki 2016). The '10 keV feature' observed in the X-ray spectra during the 2019 outburst showed a trend which is similar to that observed during the 2003 outburst of 1901. We discuss the origin of this feature later in this section. A positive correlation was observed in the energy of this feature with the X-ray flux as observed earlier (see fig. 7 of Reig & Milonaki 2016). Iron line energies showed similar values during all four observations; however, EW showed a higher value during Obs 2, indicating luminosity dependence. This is again consistent with previous reports on this source (Reig & Milonaki 2016).

5.2.2 Cyclotron line at 30 keV: magnetic field estimate, pulse phase dependence, and transient nature

One of the significant outcomes of this study is the confirmation of cyclotron line (E_{cyc}) around 30 keV in the X-ray spectra of

1901 and studying its variable nature both with luminosity and pulse phase. This feature was first detected by Coley et al. (2019); however, this is for the first time the existence of this feature has been well established. An abrupt change in the pulse profiles around this energy was observed. There have also been other sources where an abrupt change in the pulse shape near the CRSF energy has been observed, as an example V0332+53 (see Tsygankov et al. 2006, for details). The presence of a broad absorption feature in the X-ray continuum of X-ray pulsars is reminiscent of a cyclotron line absorption feature and its energy is related to the magnetic field of neutron star: $E_{cyc} = 11.6/(1 + z) B_{12}$ keV where B_{12} is the magnetic field strength in units of 10^{12} G and z is gravitational redshift (0.3 is a typical value used for standard neutron star parameters). Using this relation, we inferred magnetic field of the neutron star to be $\sim 3.5 \times 10^{12}$ G.

CRSF at 30 keV in 1901 was detected in the phase-averaged spectra of only low-luminosity observations and at certain phases

during the bright observations indicating it to be a transient feature. Coley et al. (2019) also indicated the presence of an additional narrow absorption feature around 30 keV in the *NuSTAR* spectra during the declining phase of the outburst, which was not seen in the observations made during the rising phase of the outburst.

Cyclotron line observed in the X-ray spectra originates from the accretion column (Nishimura 2014; Schönherr et al. 2014), which is highly luminosity dependent. It has also been proposed in some cases that the line can be formed as a result of the reflection of X-rays from the atmosphere of the neutron star (Poutanen et al. 2013; Lutovinov et al. 2015). Non-detection of CRSF at certain pulse phases is explained as a result of large gradient of the magnetic field strength over the visible column height or latitudes on the stellar surface (see e.g. Molkov et al. 2019). Thus, there may be the possibility that during Obs 1 and Obs 2, the 30-keV feature could be smeared out in the phase-averaged spectrum due to its large variability across the phase and the possible effects due to light bending (Falkner 2018).

An important characteristic of CRSF is its dependence on the pulse phase. Our results showed a strong dependence of 30 keV feature on the pulse phase. E_{cyc} varied by ∼60 per cent and ∼47 per cent during Obs 3 and Obs 4, respectively. The CRSF detected at certain phases of Obs 1 and Obs 2 also showed values similar to that observed during Obs 3 and Obs 4. A similar variation of CRSF has also been observed in other sources. Such variation of CRSF is understood to be a result of sampling different heights of the line-forming region as a function of pulse phase or alternatively a complex accretion geometry or a large gradient in the B field indicating a non-dipolar geometry (see Maitra 2017; Staubert et al. 2019, for details). From Fig. 14, it is also evident that optical depth shows a trend similar to the pulse profile in the energy band coinciding with the band where CRSF is identified in the spectrum of this source. Thus, this must be taken into account while constructing models of CRSFs in the neutron star atmosphere.

5.2.3 Pulse phase dependence of spectral parameters

From our pulse phase-resolved spectroscopy, we observed a negative correlation of photon index with the X-ray flux. Our HR plots also showed a correlation between intensity and hardness (Fig. 8). Thus, our spectral results are consistent with our model-independent approach to probe into the spectral evolution across the pulse phase. We observed an anticorrelation between the iron line EW and pulse profiles, which may suggest that the amount of neutral matter obscuring the neutron star is higher at the off-pulse phases that gives rise to stronger iron fluorescence lines. We observed a strong pulse phase dependence of '10 keV feature', which is consistent with that observed during previous outburst of 1901 in 2003 (Chen et al. 2008; Reig & Milonaki 2016). However, it is also believed that '10 keV feature' can also arise due to the limitation of simple phenomenological models used for describing the X-ray continuum (see Coburn et al. 2002b; Staubert et al. 2019). Moreover, our timing results (pulse profiles) did not show any significant deviation from the general trend around this energy (10 keV). This further supports our speculation that the observed '10-keV feature' may have a non-magnetic origin.

DATA AVAILABILITY

The data underlying this article are publicly available from the High Energy Astrophysics Science Archive Research Center (HEASARC), provided by NASA's Goddard Space Flight Center.

REFERENCES

Araya R. A., Harding A. K., 1999, ApJ, 517, 334
Araya-Góchez R. A., Harding A. K., 2000, ApJ, 544, 1067
Arnaud K. A., 1996, Astronomical Data Analysis Software and Systems V, series: Astronomical Society of the Pacific Conference Series , Vol. 101. p. 17
Bailer-Jones C. A. L., Rybizki J., Fouesneau M., Mantelet G., Andrae R., 2018, AJ, 156, 58
Barlow R., 1989, Statistics. A guide to the use of statistical methods in the physical sciences. Wiley, New York
Basko M. M., 1978, ApJ, 223, 268
Basko M. M., 1980, A&A, 87, 330
Becker P. A. et al., 2012, A&A, 544, A123
Beri A., Paul B., 2017, New A, 56, 94
Beri A., Jain C., Paul B., Raichur H., 2014, MNRAS, 439, 1940
Bildsten L. et al., 1997, ApJS, 113, 367
Bissinger né Kühnel M. et al., 2020, A&A, 634, A99
Burderi L., Di Salvo T., Robba N. R., La Barbera A., Guainazzi M., 2000, ApJ, 530, 429
Chen W., Qu J.-l., Zhang S., Zhang F., Zhang G.-b., 2008, Chinese Astron. Astrophys., 32, 241
Coburn W., Heindl W. A., Rothschild R. E., Gruber D. E., Kreykenbohm I., Wilms J., Kretschmar P., Staubert R., 2002a, ApJ, 580, 394
Coburn W., Heindl W. A., Rothschild R. E., Gruber D. E., Kreykenbohm I., Wilms J., Kretschmar P., Staubert R., 2002b, ApJ, 580, 394
Coley J. B. et al., 2019, Astron. Telegram, 12684, 1
Corbet R. H. D., 1986, MNRAS, 220, 1047
Devasia J., James M., Paul B., Indulekha K., 2011, MNRAS, 414, 1023
Ebisawa K., Day C. S. R., Kallman T. R., Nagase F., Kotani T., Kawashima K., Kitamoto S., Woo J. W., 1996, PASJ, 48, 425
Falkner S., 2018, doctoral thesis, Friedrich-Alexander-Universität Erlangen-Nürnberg (FAU)
Ferrigno C., Falanga M., Bozzo E., Becker P. A., Klochkov D., Santangelo A., 2011, A&A, 532, A76
Forman W., Jones C., Tananbaum H., 1976, ApJ, 206, L29
Galloway D. K., Wang Z., Morgan E. H., 2005, ApJ, 635, 1217
Harding A. K., 1994, in Holt S., Day C. S., eds, American Institute of Physics Conference Series Vol. 308, The Evolution of X-ray Binariese. p. 429
Hemphill P., Coley J., Fuerst F., Kretschmar P., Kuehnel M., Malacaria C., Pottschmidt K., 2019, Astron. Telegram, 12556, 1
Jaisawal G. K. et al., 2019, Astron. Telegram, 12515, 1
James M., Paul B., Devasia J., Indulekha K., 2011, MNRAS, 410, 1489
Jenke P., Finger M. H., 2011, Astron. Telegram, 3839, 1
Ji L. et al., 2020, MNRAS, 493, 5680
Kraus U., Nollert H. P., Ruder H., Riffert H., 1995, ApJ, 450, 763
Kraus U., Blum S., Schulte J., Ruder H., Meszaros P., 1996, ApJ, 467, 794

Kreykenbohm I., Kretschmar P., Wilms J., Staubert R., Kendziorra E., Gruber D. E., Heindl W. A., Rothschild R. E., 1999, A&A, 341, 141

Lei Y.-J., Chen W., Qu J.-L., Song L.-M., Zhang S., Lu Y., Zhang H.-T., Li T.-P., 2009, ApJ, 707, 1016

Lutovinov A. A., Tsygankov S. S., Suleimanov V. F., Mushtukov A. A., Doroshenko V., Nagirner D. I., Poutanen J., 2015, MNRAS, 448, 2175

Maitra C., 2017, J. Astrophys. Astron., 38, 50

Maitra C., Paul B., 2013, Astrophys. J., 763, 79

Maitra C., Paul B., Naik S., 2012, MNRAS, 420, 2307

Maitra C., Raichur H., Pradhan P., Paul B., 2017, MNRAS, 470, 713

McCollum B., Laine S., 2019, Astron. Telegram, 12560, 1

Mereminskiy I. A., Lutovinov A. A., Tsygankov S. S., Semena A. N., Shtykovskiy A. E., 2019, Astron. Telegram, 12514, 1

Meszaros P., Nagel W., 1985, ApJ, 298, 147

Molkov S., Lutovinov A., Grebenev S., 2003, A&A, 411, L357

Molkov S., Lutovinov A., Tsygankov S., Mereminskiy I., Mushtukov A., 2019, ApJ, 883, L11

Mushtukov A. A., Suleimanov V. F., Tsygankov S. S., Poutanen J., 2015a, MNRAS, 447, 1847

Mushtukov A. A., Suleimanov V. F., Tsygankov S. S., Poutanen J., 2015b, MNRAS, 447, 1847

Nagase F., 1989, PASJ, 41, 1

Nagel W., 1981, ApJ, 251, 288

Nakajima M. et al., 2019, Astron. Telegram, 12498, 1

Nishimura O., 2014, ApJ, 781, 30

Orlandini M., Frontera F., Masetti N., Sguera V., Sidoli L., 2012, ApJ, 748, 86

Parmar A. N., White N. E., Stella L., 1989, ApJ, 338, 373

Poutanen J., Mushtukov A. A., Suleimanov V. F., Tsygankov S. S., Nagirner D. I., Doroshenko V., Lutovinov A. e. A., 2013, ApJ, 777, 115

Priedhorsky W. C., Terrell J., 1984, ApJ, 280, 661

Reig P., 2011, Ap&SS, 332, 1

Reig P., Milonaki F., 2016, A&A, 594, A45

Reig P., Nespoli E., 2013, A&A, 551, A1

Schönherr G., Wilms J., Kretschmar P., Kreykenbohm I., Santangelo A., Rothschild R. E., Coburn W., Staubert R., 2007, A&A, 472, 353

Schönherr G. et al., 2014, A&A, 564, L8

Sootome T. et al., 2011, Astron. Telegram, 3829, 1

Staubert R. et al., 2019, A&A, 622, A61

Strader J., Chomiuk L., Swihart S., Aydi E., 2019, Astron. Telegram, 12554, 1

Tanaka Y., 1986, in Mihalas D., Winkler K.-H. A., eds, Radiation Hydrodynamics in Stars and Compact Objects. Springer, Berlin Heidelberg, p. 198

Titarchuk L., 1994, ApJ, 434, 570

Tsygankov S. S., Lutovinov A. A., Churazov E. M., Sunyaev R. A., 2006, MNRAS, 371, 19

Tsygankov S. S., Lutovinov A. A., Churazov E. M., Sunyaev R. A., 2007, Astron. Lett., 33, 368

Tuo Y. L. et al., 2020, J. High Energy Astrophys., 27, 38

Verner D. A., Ferland G. J., Korista K. T., Yakovlev D. G., 1996, ApJ, 465, 487

Wilms J., Allen A., McCray R., 2000, ApJ, 542, 914

This paper has been typeset from a TEX/LATEX file prepared by the author.